

# **Scalable and telecom single-erbium system with record-long room-temperature quantum coherence**

Alex Kaloyerros, Natasha Tabassum, and Spyros Gallis\*

College of Nanotechnology, Science, and Engineering (CNSE), Department of Nanoscale Science and Engineering, University at Albany (UAlbany), NY 12222, USA

\*Corresponding Author: sgalis@albany.edu

Eliminating cryogenic operating requirements while preserving microsecond-scale quantum coherence and enabling CMOS scalability remains a central challenge for telecom quantum technologies. Addressing this, we introduce a CMOS-compatible quantum system comprising single-erbium-( $\text{Er}^{3+}$ )-ion qudits (five-level systems) operating across the visible and telecom C-band. Through innovative nanofabrication, we achieve self-aligned ion placement, enabling spatial isolation of single- $\text{Er}^{3+}$  ions and suppressing dephasing. We realize individually addressable single-Er-devices with record-long optical coherence times in the telecom C-band exceeding 500  $\mu\text{s}$  at ambient conditions, a performance previously limited to vacuum conditions at temperatures over 900 times lower. Furthermore, we present the first demonstration of background-free, upconversion-enabled single-photon Er-emissions providing coherent, high-contrast optical readouts. This work showcases the first room-temperature single-Er-qudit system with unprecedented properties enabling next-generation cryogen-free telecom quantum technologies.

Advancing quantum information science (QIS) - including sensing, photonics, information processing, and communications - demands innovative materials engineering to overcome persistent limitations of quantum systems such as cryogenic operation, rapid decoherence at elevated temperatures, and limited scalability.<sup>1,2,3,4,5</sup> Thus, an interrelated challenge is to develop solid-state quantum systems that retain microsecond-scale<sup>6</sup> quantum coherence at higher temperatures, ideally reaching room temperature (RT), while simultaneously supporting scalable, CMOS (complementary metal-oxide semiconductor)-compatible fabrication and telecom C-band operation. Tackling this challenge is essential for transitioning from laboratory prototypes to practical, on-chip quantum systems, including quantum photonic integrated circuits (qPICs).<sup>7,8,9</sup> Such integration, which merges optical and electrical functionalities on a unified platform, is critical for scalability and manufacturability, mirroring the transformative role of integrated circuits in classic semiconductor technology. Moreover, deployable quantum systems must be designed to reduce size, weight, power consumption, and cost (SWaP+C) to be effectively used in real-world settings.<sup>3</sup> On-chip quantum systems, based on telecom quantum emitters and qubits (including, potentially, higher-dimensional qudits, with  $d > 2$  energy levels) that operate in the low-loss telecom band (e.g., the C-band around 1540 nm) and are compatible with fiber networks,<sup>6,10,11</sup> form the technological foundation of next-generation QIS applications, such as long-distance quantum networking, quantum information storage and processing, and distributed quantum sensing and computing.<sup>12,13</sup>

In this landscape, a range of solid-state quantum systems, such as semiconductor quantum dots,<sup>14,15,16</sup> defects,<sup>17,18,19</sup> and rare-earth-erbium ( $\text{Er}^{3+}$ ) ions<sup>4,20,21,22,23,24,25,26</sup>, have enabled pioneering demonstrations of quantum functionality, such as state-of-the-art sensitivities<sup>27,28</sup> in measuring magnetic and electric fields in the near infrared range (1000 nm – 1300 nm), deterministic single-photon emission, spin-photon interfaces<sup>20,24</sup> and more importantly microsecond-scale quantum-coherence and high-fidelity optical control in the telecom C-band,<sup>29,30,31</sup> albeit under controlled laboratory vacuum conditions at cryogenic temperatures below 0.5 K. Thus, scaling these systems beyond the lab remains challenging due either to stringent operating conditions, a lack native telecom C-band operation, and/or limited compatibility with large-scale fabrication, constraints that fundamentally limit their suitability for practical, low SWaP+C quantum technologies. Furthermore, environmental factors such as mechanical vibrations and fluctuating electromagnetic fields arising from defects, charge noise, and spin-bath interactions, further degrade coherence and stability in realistic device environments. **Table S1 in the Supplementary** highlights the absence of a unified solution by summarizing these trade-offs across these quantum systems (e.g., telecom-band

operation, CMOS-compatible fabrication, and state-of-the-art creation and control of coherence above cryogenic temperatures), motivating the novel materials and quantum engineering approach introduced in this work.

In addressing this, we demonstrate a groundbreaking foundry-compatible nanofabrication, paired with targeted materials engineering, that enables the realization of a new class of CMOS-scalable solid-state quantum systems: arrays of spatially-isolated single- $\text{Er}^{3+}$ -ion qudits embedded in silicon carbide (SiC)-based hollow nanopillars (HNPs). This is achieved via non-lithographically defined nanostructure geometries with ultrathin critical dimensions ( $\leq 5$  nm), which impose a geometric-based confinement that self-aligns and spatially isolates individual  $\text{Er}^{3+}$  ions. SiC was selected as the host matrix for  $\text{Er}^{3+}$  due to its unique fundamental and technological advantages.<sup>32,33</sup> For example, amorphous-SiC-on-insulator (a-SiCOI)<sup>34</sup> offers CMOS compatibility, a wide bandgap, a high refractive index ( $n \approx 2.6$  at 1550 nm), and strong electro-optic properties.<sup>34,35</sup> Within our HNP devices, we observe a three-order of magnitude increase in the excitation cross-section ( $\sigma$ ) for single- $\text{Er}^{3+}$ -ions, enabling their isolation and coherent optical control under ambient conditions - capabilities that have previously required nanophotonic cavities and cryogenic temperatures ( $\leq 0.5$  K) for spectral isolation of Er ions.<sup>23,24</sup> The sub-5 nm critical dimensions of the HNP arrays create an environment where spatially-isolated single- $\text{Er}^{3+}$ -ions are effectively suspended in “air”, substantially suppressing ion-ion interactions and mitigating spectral diffusion and decoherence from defects and fluctuating charges.

Our quantum devices exhibit exceptional performance at room temperature that are unattainable in current technologies. We demonstrate coherent operation in the telecom C-band with record-long optical quantum coherence exceeding 500  $\mu\text{s}$ ,<sup>4,20,22,36</sup> measured by standard photon-echo pulse sequences. Furthermore, we exploit the multi-energy level structure of the spatially isolated single-Er-qudits ( $d = 5$ -level system) to realize a high-Q (exhibiting a narrow linewidth and long coherence time), background-free, single photon emission via an upconversion-mediated readout pathway. This approach enables fast, high-contrast (>96%) coherent optical readout in the visible (e.g., 518 nm) without the use of an optical cavity. Together, these results establish a comprehensive telecom- and CMOS-compatible engineering strategy, enabled by materials science and engineering, that overcomes the ubiquitous challenge of maintaining quantum coherence under ambient conditions, enabling operation at temperatures more than 900-times higher than those required by cryogenic quantum systems. This work paves the way for

advanced telecom QIS technologies that could potentially extend the range of practical applications in quantum sensing and imaging for biomedical applications, and in quantum sensing and reference systems (clock synchronization, distributed computation)<sup>3</sup> for a future Quantum Internet of Things.<sup>37</sup>

Figure 1 outlines the fabrication strategy and key-enabling innovations underlying the Er-doped SiC-based HNP array platform, which is realized without a conventional lithographic pattern-transfer. Building on our previously reported approach for Er-doped SiC nanowire (NW) structures<sup>38</sup>, this approach advances beyond ensemble implantation towards the creation and control of single Er<sup>3+</sup> ions. Innovation 1 (**Figure 1B**) demonstrates the non-lithographic route for defining SiC-based HNPs with  $\leq 5$  nm critical dimension (C.D.), achieved through a conformal chemical vapor deposition (CVD) process<sup>39</sup> with accurately-controlled growth rates of  $\sim 0.3$  Å/s. A sacrificial mandrel patterned by electron-beam lithography (pink in **Figure 1A**) serves only as a geometric scaffold, while the final nanostructure dimensions are set by the thickness of a conformally deposited  $\leq 5$ -nm-thick amorphous SiC (a-SiC) layer, or oxygen co-doped a-SiC layer (a-SiC:O),<sup>38</sup> deposited on the mandrel which defines the nanostructure dimensions independent of lithographic resolution (see Materials and Methods in the Supplemental). Subsequent selective reactive-ion etching yields hollow stoichiometric a-SiC (and a-SiC:O) HNPs with smooth, uniform sidewalls, and sub-5-nm C.D.s, exhibiting minimal surface roughness ( $\sim 2$  Å). By decoupling C.D. control from lithography and avoiding the typical etching steps in top-down nanofabrication, our scheme circumvents conventional lithographic resolution limits and minimizes sidewall roughness, two inherent challenges in lithographic-pattern-transfer nanofabrication.<sup>40</sup>

Deterministic integration of single ions with nanometer-scale spatial accuracy,<sup>41</sup> is a central requirement for scalable single-ion qubits/qudits, as on-demand spatial isolation can enable scalability and enhanced coherent control.<sup>42,43</sup> We achieve this by exploiting the geometry of the HNP whose C.D. ( $\leq 5$  nm) enable geometry-defined ion placement with state-of-the-art ( $< 5$  nm) accuracy (Innovation 2, **Figure 1C**). In this implantation scheme, the HNP sidewall functions as a lateral implantation aperture that constrains the final ion placement volume. Following removal of a sacrificial oxide present during implantation, implanted Er ions are confined within the SiC-based HNP nanostructures (hereafter referred to as Er:SiC HNP or Er:SiC NW). Unlike conventional approaches that rely on lithographic alignment, the physical dimensions of the HNPs impose self-aligned nanoscale confinement, suppressing stochastic ion positioning and enabling deterministic ion placement compatible with wafer-scale fabrication. This geometry-defined confinement strategy

is broadly applicable to any class of ion or defect introduced via implantation. Control over ion placement is ensured through a dedicated metrology sequence that determines the etch-stopping point and the overlap between the implanted Er depth profile and the HNP height (see further details in **Supplemental Information**). Room-temperature (RT) resonant-telecom photoluminescence-excitation (PLE) spectroscopy on a representative single-Er<sup>3+</sup> in a 3×4 HNP array device reveals a transition centered at ~1533.9 nm within the telecom C-band, with a measured linewidth of ~67 MHz (**Figure 1C iii**), limited by the frequency-modulation broadening of the tunable telecom C-band laser<sup>44</sup> (see also the Supplemental Information). Subsequent RT pulsed second-order photon-correlation (pulsed- $g^2(\tau)$ ) measurements performed under resonant telecom excitation exhibited clear antibunching with  $g^2(0) = 0.35 \pm 0.04$ , confirming single-photon emission from a spatially isolated Er<sup>3+</sup> ion. To our knowledge, this constitutes the first demonstration of room-temperature spatially-resolved isolation of single-Er<sup>3+</sup>-ions without reliance on spectral isolation using a nanophotonic cavity.<sup>20,23,24,45</sup>

To determine optimal implantation parameters, we employed stopping-and-range-of-ions-in-matter (SRIM) simulations to model the depth distribution of implanted Er ions and accompanying profile of implantation-induced lattice damage. This SRIM-based framework for minimizing implantation-induced defects has been experimentally validated in our previous report on Er-implanted thin-film lithium niobate (Er:LN).<sup>46</sup> These simulations provide quantitative predictions linking implantation depth to regions with elevated implantation-induced vacancies, represented by an effective density of vacancies estimated within the Er ions' immediate interaction volume. By correlating the simulated vacancy concentration with the implantation energy and oxide encapsulation thickness, we can select conditions to achieve the target Er depth placement while minimizing defectivity.

We combine these nanofabrication innovations with a materials-engineering strategy that enables efficient optical probing of few and single Er<sup>3+</sup> ions at room temperature. As previously reported,<sup>38,47,48</sup> Er-implanted a-SiC:O thin-films and nanostructures exhibit broadband and efficient excitation of Er<sup>3+</sup>, mediated by matrix-assisted energy transfer.<sup>47</sup> Oxygen co-doping during SiC growth introduces C-related oxygen (O) defect centers (Si-C-O centers)<sup>47,49,50</sup> which facilitate the transfer process through energy states that overlap with the Er<sup>3+</sup> excited-state manifold.<sup>38,47</sup> Consistent with this, ensemble Er<sup>3+>:SiC HNP arrays exhibit broadband excitation with an effective excitation cross-section  $\sigma \approx 2 \times 10^{-17} \text{ cm}^2$ , representing a 2-3 orders-of-magnitude enhancement compared to typical</sup>

benchmark values in bulk host materials. Power-dependence photoluminescence (PDPL) and PLE measurements confirm an efficient broadband energy-transfer mechanism<sup>51</sup> between the nanostructured matrix and Er<sup>3+</sup> ions, as the Er<sup>3+</sup> emission can be sensitized by the nanostructured SiC matrix (**Figure 2A, B**). Additional enhancement may arise from effective light trapping in the HNP array due to multiple scattering, increasing absorption probability of excitation light. In contrast, Er<sup>3+</sup>-implanted LN and SiO<sub>2</sub> reference samples<sup>46</sup> exhibit detectable excitation only under direct resonant excitation at the Er<sup>3+</sup> optical transition wavelengths with  $\sigma \approx 6 \times 10^{-20} \text{ cm}^2$ . **Figure 2B** highlights the impact of the enhanced excitation cross section by comparing resonant telecom PDPL measurements from a representative Er:SiC HNP array containing  $\sim 5$  Er<sup>3+</sup> ions with those from a LN reference sample containing the same number of ions. The Er:SiC HNP device exhibits a strong PL signal that exceeds SNSPD detection thresholds and saturates at significantly lower photon flux ( $\phi \sim 10^{21} \text{ cm}^{-2} \cdot \text{s}^{-1}$ ), whereas emission from the LN reference remains essentially undetectable even at the highest excitation photon flux used in the experiments ( $\phi > 10^{22} \text{ cm}^{-2} \cdot \text{s}^{-1}$ ). These results establish that the Er:SiC HNP platform substantially enhances excitation efficiency, enabling room-temperature single-Er<sup>3+</sup>-ion detection (**Figure 1C iv**), without spectroscopically resolving them in nanocavities at  $\leq 0.5$  K.

To engineer the conditions necessary for single-ion isolation, we developed a geometry- and dose-based design blueprint that quantitatively correlates implantation dose, post-implantation processing, and nanostructure volume. As either the implantation dose or the effective nanostructure volume is reduced, the probability distribution of Er<sup>3+</sup> ions within the optical excitation volume transitions from a many-emitter ensemble to a regime dominated by single-ion probability. This concept is illustrated schematically in **Figure 3A** (see also **Supplemental Figures S4 and S5**), where systematic tuning of the implantation dose (y-axis) and nanostructure geometry and C.D. (x-axis) reduces the expected number of Er<sup>3+</sup> ions ( $N_{\#}$ ) within a diffraction-limited excitation spot. **Figure 3B** summarizes the representative nanostructure arrays investigated in this study together with the calculated number of excited Er<sup>3+</sup> ions for each configuration. Using this framework, we achieve predetermined and targeted  $N_{\#}$  of implanted ions, including single-ion isolation, in the HNP1 arrays with a C.D. of 4.8 nm and Er-implantation dose of  $10^{12} \text{ cm}^{-2}$ . To mitigate the inherently stochastic nature of ion implantation and improve experimental yield, the HNP1 arrays were designed to include multiple HNPs (12) within a single excitation beam, thereby increasing the probability of single-ion detection while preserving confinement. Each HNP1 array comprises a  $10^3 \times 10^3$  lattice of HNPs distributed over a  $250 \times 250 \mu\text{m}^2$  area with a 250 nm pitch, yielding approximately 12 HNPs (4×3 HNPs

array) within the telecom C-band diffraction-limited excitation beam spot (**Figure 3C i**). Three representative arrays (A1 - A3), implanted with progressively reduced targeted  $\text{Er}^{3+}$  numbers ranging from  $\sim 10$  ions (A1) to  $\sim 2$  ions (A3) per excitation volume, were used to establish a controlled testbed for quantum emission studies (**Figure 3C ii** and **Supplemental Figure S7**). Pulsed- $g^2(\tau)$  measurements on representative sites on arrays A1 (S1) and A3 (S3) revealed antibunching, confirming quantum emission. Fitting the correlation functions using the standard pulsed- $g^2(\tau)$  model (**Supplemental Information**)<sup>52</sup> yield  $g^2(0)$  values consistent with the targeted  $N_{\#}$  (where  $g^2(0) = (N_{\#} - 1)/N_{\#}$ ), as Site S1 showed  $g^2(0) = 0.84$  ( $\sim 6$  emitters), and S3 showed  $g^2(0) = 0.38$  ( $\sim 1$  emitter).

To directly probe single-ion quantum behavior, isolated emission sites in array A4 (targeted  $N_{\#} = 1$ ) were identified via novel upconversion-mediated confocal PL mapping (**Figure 4A** and **Supplemental Figure S8**). Pulsed- $g^2$  measurements performed on a representative site Q1 under telecom-resonant excitation exhibit pronounced antibunching with  $g^2(0) = 0.25 \pm 0.03$ , confirming single-photon emission of targeted spatially-isolated single- $\text{Er}^{3+}$  ion (**Figure 4B**). Telecom time-resolved PL (TRPL) measurements reveal a biexponential decay with components  $\tau_1 = 0.3$  ms and  $\tau_2 = 1.3$  ms, yielding an average excited-state lifetime of 1.2 ms. Telecom PDPL measurements further yield an effective excitation cross section of  $\sigma = 5 \times 10^{-17} \text{ cm}^2$  and a saturation photon flux  $\phi_{\text{sat}} = 2 \times 10^{19} \text{ cm}^{-2} \text{ s}^{-1}$  (corresponding to a saturation power  $P_{\text{sat}}$  of 1 W/cm<sup>2</sup>; **Supplemental Figure S9**) consistent with the ensemble ( $N_{\#} = 5$  ions) Er:SiC HNP structures (**Figure 2B**). The ultra-thin HNP geometry ( $\leq 5$  nm) provides strong spatial isolation of individual  $\text{Er}^{3+}$  ions, suppressing ion-ion interactions and reducing defect- and charge-induced spectral diffusion, thereby enabling coherent optical control at room temperature. Under telecom-resonant pulsed excitation, coherence Rabi oscillations are observed from single  $\text{Er}^{3+}$  ions by varying the excitation pulse width  $t_p$  at a fixed photon flux ( $\phi = 6 \times 10^{19} \text{ cm}^{-2} \cdot \text{s}^{-1}$ ), with the time-integrated PL intensity recorded as a function of  $t_p$  (**Figure 4C**). The resulting oscillations were then fit using

$$I(t_p) = A \sin(\Omega_{\text{Rabi}} t_p) + B,$$

where  $t_p$  is the pulse width,  $\Omega$  is the Rabi frequency, and  $A, B$  are fitting parameters. From this fit, a Rabi frequency,  $\Omega_{\text{Rabi}}$ , of 660 kHz was extracted, demonstrating coherent optical control of a single- $\text{Er}^{3+}$  ion at ambient conditions. Correspondingly, Ramsey measurements were performed at room temperature under telecom-resonant excitation (**Figure 4D**). The Ramsey sequence consists of two  $\pi/2$  pulses, each with a width of 320  $\mu\text{s}$ , determined from the Rabi studies, separated by a variable free-evolution interval  $\tau_{\text{free}}$  (**Supplementary Figure S14**). The Ramsey signal decays exponentially

with increasing  $\tau_{\text{free}}$ , with the decay time of this projection amplitude corresponding to characteristic  $T_2^*$  coherence time. Fitting the exponential envelope to  $e^{-\frac{\tau_{\text{free}}}{T_2^*}}$  yields an optical quantum coherence time,  $T_2^*$ , of  $32 \mu\text{s} \pm 4 \mu\text{s}$ . Subsequent photon-echo measurements as a function of free-evolution time ( $\tau_{\text{free}}$ ), with an additional  $\pi$  pulse at the center of  $\tau_{\text{free}}$  used to refocus dephasing, were also performed (**Figure 4E and Supplemental Figure S14**). Fitting the data with an envelope ( $e^{-\frac{\tau_{\text{free}}}{T_2}}$ ) yields a  $T_2$  of  $568 \pm 61 \mu\text{s}$ . The single-exponential behavior indicates that decoherence of the single- $\text{Er}^{3+}$  ion in HNP devices under pulsed optical excitation is predominantly governed by pulse-excitation-induced effects and subsequent radiative relaxation dynamics.<sup>53</sup> The observed record-long coherence time of  $\sim 568 \mu\text{s}$  under ambient conditions demonstrates the suppression of fast dephasing pathways in our Er:SiC HNP and showcases that quantum coherence can be preserved even in the absence of cryogenic cooling. As mentioned above, the intrinsic optical linewidth of the single  $\text{Er}^{3+}$  in SiC HNP is limited by the broadening of the tunable-telecom-laser. However, based on the observed optical coherence time of  $T_2^* = 32 \mu\text{s}$ , the intrinsic optical linewidth is projected to be on the order of tenths of kHz ( $\Delta\nu_0 = \frac{1}{\pi T_2^*} = \sim 10 \text{ kHz}$ ).

We have implemented an upconversion-mediated pulse-sequence protocol to establish a background-free, high-efficiency optical readout pathway single-ion qudits (Er:SiC HNPs) and to access the multilevel structure of the qudit devices ( $d = 5$ -level system) (**Figure 5**). In this scheme, resonant telecom-excitation at  $\sim 1533.9 \text{ nm}$  using a sequence of  $N \pi$  pulses ( $N = 2\text{-}6$ ) populates higher-lying excited states, giving rise to visible and near-infrared upconversion emission at  $\sim 518 \text{ nm}$ ,  $\sim 660 \text{ nm}$ , and  $\sim 980 \text{ nm}$ . The corresponding energy-level diagram in **Figure 5A** illustrates the potential excitation pathways, for example, of the  $^2H_{11/2}$  manifold resulting in the  $\sim 518 \text{ nm}$  emission. **Figure 5B** shows representative results from an isolated single-ion qudit (Q1). Upconverted PL at each wavelength is selectively collected using a corresponding bandpass filter and detected with a low-light single-photon camera (Andor DV437), enabling spatially resolved imaging of individual qudits with sub-diffraction resolution ( $< 60 \text{ nm}$ ), limited by the camera pixel resolution (**Figure 5B i**). TRPL measurements of the upconverted emission yield lifetimes of  $164 \mu\text{s}$ ,  $310 \mu\text{s}$ , and  $700 \mu\text{s}$  for the  $518 \text{ nm}$ ,  $660 \text{ nm}$ , and  $980 \text{ nm}$  channels, respectively (**Figure 5B iii**). These lifetimes are substantially shorter than the  $1.2 \text{ ms}$  lifetime of the  $^4I_{13/2}$  state, consistent with radiative decay from higher-lying excited states involved in the upconversion process. PLE spectroscopy of the upconverted emission (shown representatively for the  $660 \text{ nm}$  emission) yields an optical linewidth of  $\sim 37 \text{ MHz}$ , which is

limited by the broadening of the excitation laser (**Figure 5C**).<sup>44</sup> This readout pathway supports coherent optical control, as evidenced by upconversion-mediated Rabi oscillations from individual Er<sup>3+</sup> ions (**Figure 5D**). Pulsed- $g^2$  measurements of the upconverted emissions reveal, for the first time, enhanced high-Q single-photon Er-emissions. Representative examples are presented in **Figure 5E** for the 518 nm and 980 nm upconversion states, exhibiting enhanced  $g^2(0)$  values of 0.18 and 0.12, respectively, reflecting reduced background contributions and improved signal-to-noise.

This work demonstrates the first CMOS-compatible platform of deterministic single-Er-ion qudits with record-long coherent control at room temperature in the telecom C-band. By integrating single-Er<sup>3+</sup>-ions into our sub-5 nm SiC HNPs devices, we overcome long-standing barriers to cryogenic operation, stochastic emitter placement, and non-scalable fabrication. Additionally, our quantum devices uniquely combine enhanced excitation efficiency with background-free, high-Q upconversion-mediated single-photon emissions, as demonstrated in Ramsey and photon statistics measurements, establishing a pathway toward deployable, cryogenic-free qPICs for practical, scalable quantum technologies.

## Acknowledgments

The authors gratefully acknowledge Souryaya Dutta and Kazy Shariar for their assistance with materials growth, CMP, and etching during nanofabrication of the samples. This work was also supported by the College of Nanotechnology, Science, and Engineering of the University (CNSE) Innovation Lab. **Funding.** S.G. and A.K. were supported by the U.S. National Science Foundation under Award No. 2138174.

## Author Contributions

S.G. conceived and designed the experiments and methodology, including device nanofabrication, materials engineering, and quantum optics. A.K. and S.G. developed the experimental setup. A.K. fabricated the devices, performed the measurements, and analyzed the data. N.T. assisted with the growth, preparation, and measurements of 1st-generation nanostructures. S.G. assisted in device fabrication and quantum optics measurements. S.G. contributed to data analysis and advised on all efforts. A.K. and S.G. prepared the manuscript.

## Competing interests

Three patent applications relating to this technology and innovations have been filed with the United States Patent & Trademark Office and are assigned to the Research Foundation for SUNY. Patents-pending.

## Data Availability Statement

The original contributions presented in this study are included in the article and supplementary material. Further inquiries can be directed to the corresponding author.

---

<sup>1</sup>D. Awschalom, H. Christen, A. Clerk, P. Denes, M. Flatté, D. Freedman, G. Galli, S. Jesse, M. Kasevich, C. Monroe, W. Oliver, C. Palmstrøm, Nitin Samarth, D. Schloss, I. Siddiqi, T. Taylor, B. Whaley, Amir Yacoby, J. Ye, L. Horton, Basic Energy Sciences Roundtable: Opportunities for Basic Research for Next-Generation Quantum Systems. *OSTI OAI (U.S. Department of Energy Office of Scientific and Technical Information)* (2017), doi:<https://doi.org/10.2172/1616258>.

<sup>2</sup> K. Alexander, Avishai Benyamin, D. Black, D. Bonneau, S. Burgos, B. Burridge, H. Cable, G. Campbell, G. Catalano, A. Ceballos, C.-M. Chang, S. S. Choudhury, C. Chung, F. Danesh, T. Dauer, M. Davis, E. Dudley, P. Er-Xuan, J. Fargas, Alessandro Farsi, A manufacturable platform for photonic quantum computing. *Nature* (2025), doi:<https://doi.org/10.1038/s41586-025-08820-7>.

<sup>3</sup> “Strategic Research and Industry Agenda,” (available at <https://qt.eu/media/pdf/Strategic-Reseach-and-Industry-Agenda-2030.pdf>).

<sup>4</sup> R. M. Pettit, Skylar Deckoff-Jones, A. Donis, A. Elias, J. Briscoe, G. Leake, D. Coleman, M. Fanto, Ananthesh Sundaresh, S. Gupta, M. K. Singh, S. E. Sullivan, Monolithically Integrated C-Band Quantum Emitters on Foundry Silicon Photonics. *Nano Letters*. 25, 11803–11810 (2025).

---

<sup>5</sup> M. Sartison, O. C. Ibarra, Ioannis Caltzidis, D. Reuter, K. D. Jöns, Scalable integration of quantum emitters into photonic integrated circuits. *Materials for Quantum Technology*. 2, 023002–023002 (2022).

<sup>6</sup> Miloš Rančić, M. Hedges, R. Ahlefeldt, M. Sellars, Coherence time of over a second in a telecom-compatible quantum memory storage material. *Nature Physics*. 14, 50–54 (2017).

<sup>7</sup> Anastasiia Zalogina, N. Coste, C. Chen, J. Kim, Igor Aharonovich, Engineering Quantum Light: Emitters, Photonic Structures, and On-Chip Integration. *Laser & Photonics Review* (2025), doi:<https://doi.org/10.1002/lpor.202502309>.

<sup>8</sup> E. Pelucchi, G. Fagas, I. Aharonovich, D. Englund, E. Figueroa, Q. Gong, H. Hannes, J. Liu, C.-Y. Lu, N. Matsuda, J.-W. Pan, F. Schreck, F. Sciarrino, C. Silberhorn, J. Wang, K. D. Jöns, The potential and global outlook of integrated photonics for quantum technologies. *Nature Reviews Physics*. 4, 194–208 (2022).

<sup>9</sup> A. H. Atabaki, S. Moazeni, F. Pavanello, H. Gevorgyan, J. Notaros, L. Alloatti, M. T. Wade, C. Sun, S. A. Kruger, H. Meng, K. Al Qubaisi, I. Wang, B. Zhang, A. Khilo, C. V. Baiocco, M. A. Popović, V. M. Stojanović, R. J. Ram, Integrating photonics with silicon nanoelectronics for the next generation of systems on a chip. *Nature*. 556, 349–354 (2018).

<sup>10</sup> K. Azuma, S. E. Economou, D. Elkouss, P. Hilaire, L. Jiang, H.-K. Lo, Ilan Tzitrin, Quantum repeaters: From quantum networks to the quantum internet. *arXiv* (Cornell University) (2022), doi:<https://doi.org/10.1103/revmodphys.95.045006>.

<sup>11</sup> E. Saglamyurek, J. Jin, V. B. Verma, M. D. Shaw, F. Marsili, S. W. Nam, D. Oblak, W. Tittel, Quantum storage of entangled telecom-wavelength photons in an erbium-doped optical fibre. *Nature Photonics*. 9, 83–87 (2015).

<sup>12</sup> H. J. Kimble, The quantum internet. *Nature*. 453, 1023–1030 (2008).

<sup>13</sup> J. L. O'Brien, A. Furusawa, J. Vučković, Photonic quantum technologies. *Nature Photonics*. 3, 687–695 (2009).

<sup>14</sup> Y. Yu, S. Liu, C.-M. Lee, P. Michler, S. Reitzenstein, K. Srinivasan, E. Waks, J. Liu, Telecom-band quantum dot technologies for long-distance quantum networks. *Nature Nanotechnology*. 18, 1389–1400 (2023).

<sup>15</sup> M. Anderson, T. Müller, J. Huwer, J. Skiba-Szymanska, A. B. Krysa, R. M. Stevenson, J. Heffernan, D. A. Ritchie, A. J. Shields, Quantum teleportation using highly coherent emission from telecom C-band quantum dots. *npj Quantum Information*. 6 (2020), doi:<https://doi.org/10.1038/s41534-020-0249-5>.

<sup>16</sup> K. D. Zeuner, M. Paul, T. Lettner, C. Reuterskiöld Hedlund, L. Schweickert, S. Steinhauer, L. Yang, J. Zichi, M. Hammar, K. D. Jöns, V. Zwiller, A stable wavelength-tunable triggered source of single photons and cascaded

---

photon pairs at the telecom C-band. *Applied Physics Letters.* 112 (2018), doi:<https://doi.org/10.1063/1.5021483>.

<sup>17</sup> Q. Li, J.-F. Wang, F.-F. Yan, J.-Y. Zhou, H.-F. Wang, H. Liu, L.-P. Guo, X. Zhou, A. Gali, Z.-H. Liu, Z.-Q. Wang, K. Sun, G.-P. Guo, J.-S. Tang, H. Li, L.-X. You, J.-S. Xu, C.-F. Li, G.-C. Guo, Room-temperature coherent manipulation of single-spin qubits in silicon carbide with a high readout contrast. *National Science Review.* 9 (2021), doi:<https://doi.org/10.1093/nsr/nwab122>.

<sup>18</sup> P. Cilibrizzi, M. J. Arshad, B. Tissot, N. T. Son, I. G. Ivanov, T. Astner, P. Koller, Misagh Ghezelou, Jawad Ul-Hassan, D. White, C. Bekker, G. Burkard, M. Trupke, C. Bonato, Ultra-narrow inhomogeneous spectral distribution of telecom-wavelength vanadium centres in isotopically-enriched silicon carbide. *Nature Communications.* 14, 8448–8448 (2023).

<sup>19</sup> M. Atatüre, D. Englund, N. Vamivakas, S.-Y. Lee, J. Wrachtrup, Material platforms for spin-based photonic quantum technologies. *Nature Reviews Materials.* 3, 38–51 (2018).

<sup>20</sup> L. Yang, S. Wang, M. Shen, J. Xie, H. X. Tang, Controlling single rare earth ion emission in an electro-optical nanocavity. *Nature Communications.* 14 (2023)

<sup>21</sup> Y. Yu, D. Oser, G. D. Prato, E. Urbinati, J. C. Ávila, Y. Zhang, P. Remy, S. Marzban, S. Gröblacher, W. Tittel, Frequency Tunable, Cavity-Enhanced Single Erbium Quantum Emitter in the Telecom Band. *Physical Review Letters.* 131, 170801–170801 (2023).

<sup>22</sup> I. R. Berkman, A. Lyasota, G. G. de Boo, J. G. Bartholomew, S. Q. Lim, B. C. Johnson, J. C. McCallum, B.-B. Xu, S. Xie, N. V. Abrosimov, H.-J. Pohl, R. L. Ahlefeldt, M. J. Sellars, C. Yin, S. Rogge, Long optical and electron spin coherence times for erbium ions in silicon. *npj Quantum Information.* 11 (2025), doi:<https://doi.org/10.1038/s41534-025-01008-x>.

<sup>23</sup> S. Ourari, Ł. Dusanowski, S. P. Horvath, M. T. Uysal, C. M. Phenicie, P. Stevenson, M. Raha, S. Chen, R. J. Cava, N. P. de Leon, J. D. Thompson, Indistinguishable telecom band photons from a single Er ion in the solid state. *Nature.* 620, 977–981 (2023).

<sup>24</sup> L. R. Weiss, G. T. Smith, R. A. Murphy, Bahman Golesorkhi, José A. Méndez Méndez, P. Patel, J. Niklas, O. G. Poluektov, J. R. Long, D. D. Awschalom, A high-resolution molecular spin-photon interface at telecommunication wavelengths. *Science.* 390, 76–81 (2025).

<sup>25</sup> S. Gupta, R. M. Pettit, A. Sundaresh, V. Niaouris, S. Deckoff-Jones, D. P. Crowley, L. G. Carpenter, A. M. Dibos, M. K. Singh, S. E. Sullivan, Erbium quantum memory platform with long optical coherence via back-end-of-line deposition on foundry-fabricated photonics. *Physical Review Applied.* 24 (2025), doi:<https://doi.org/10.1103/xj8y-b6sl>.

---

<sup>26</sup> S. Wang, L. Yang, M. Shen, W. Fu, Y. Xu, R. L. Cone, C. W. Thiel, H. X. Tang, Er :Li:Nb:O<sub>3</sub> with High Optical Coherence Enabling Optical Thickness Control. *Physical Review Applied*. 18 (2022), doi:<https://doi.org/10.1103/physrevapplied.18.014069>.

<sup>27</sup> S Castelletto, C T-K Lew, W.-X. Lin, J.-S. Xu, Quantum systems in silicon carbide for sensing applications. *Reports on progress in physics*. 87, 014501–014501 (2023).

<sup>28</sup> C. P. Anderson, A. Bourassa, K. C. Miao, G. Wolfowicz, P. J. Mintun, A. L. Crook, H. Abe, Jawad Ul Hassan, N. T. Son, Takeshi Ohshima, D. D. Awschalom, Electrical and optical control of single spins integrated in scalable semiconductor devices. *Science*. 366, 1225–1230 (2019).

<sup>29</sup> S. Wehner, D. Elkouss, R. Hanson, Quantum internet: A vision for the road ahead. *Science*. 362, eaam9288 (2018).

<sup>30</sup> C. Yin, Miloš Rančić, Gabriele, N. Stavrias, J. C. McCallum, M. J. Sellars, S. Rogge, Optical addressing of an individual erbium ion in silicon. *Nature*. 497, 91–94 (2013).

<sup>31</sup> D. D. Awschalom, R. Hanson, J. Wrachtrup, B. B. Zhou, Quantum technologies with optically interfaced solid-state spins. *Nature Photonics*. 12, 516–527 (2018).

<sup>32</sup> D. Lukin, C. Dory, M. A. Gidry, Ki Youl Yang, Sattwik Deb Mishra, R. Trivedi, M. Radulaski, S. Sun, D. Vercruyse, Geun Ho Ahn, J. Vuckovic, 4H-silicon-carbide-on-insulator for integrated quantum and nonlinear photonics. *Nature Photonics*. 14, 330–334 (2019).

<sup>33</sup> A. Lohrmann, B. M. Johnson, J. C. McCallum, S. Castelletto, A review on single photon sources in silicon carbide. *Reports on Progress in Physics*. 80, 034502–034502 (2017).

<sup>34</sup> S. Dutta, A. Kaloyerous, A. Nanaware, S. Gallis, Scalable Chemical Vapor Deposition of Silicon Carbide Thin Films for Photonic Integrated Circuit Applications. *Applied Sciences*. 15, 8603 (2025).

<sup>35</sup> A. Yi, C. Wang, L. Zhou, M. Zhou, S. Zhang, T. You, J. Zhang, X. Ou, Silicon carbide for integrated photonics. *Applied physics reviews*. 9 (2022), doi:<https://doi.org/10.1063/5.0079649>.

<sup>36</sup> J. Wong, M. Onizhuk, J. Nagura, A. S. Thind, J. K. Bindra, C. Wicker, G. D. Grant, Y. Zhang, J. Niklas, O. G. Poluektov, R. F. Klie, J. Zhang, G. Galli, F. J. Heremans, D. D. Awschalom, A. P. Alivisatos, Coherent Erbium Spin Defects in Colloidal Nanocrystal Hosts. *ACS Nano*. 18, 19110–19123 (2024).

<sup>37</sup> A. Singh, K. Dev, H. Siljak, H. D. Joshi, M. Magarini, Quantum Internet—Applications, Functionalities, Enabling Technologies, Challenges, and Research Directions. *IEEE Communications Surveys & Tutorials*. 23, 2218–2247 (2021).

---

<sup>38</sup> N. Tabassum, V. Nikas, A. E. Kaloyerous, V. Kaushik, E. Crawford, M. Huang, S. Gallis, Engineered telecom emission and controlled positioning of Er<sup>3+</sup> enabled by SiC nanophotonic structures. *Nanophotonics*. 9, 1425–1437 (2020).

<sup>39</sup> N. Tabassum, M. Kotha, V. Kaushik, B. Ford, S. Dey, E. Crawford, V. Nikas, S. Gallis, On-Demand CMOS-Compatible Fabrication of Ultrathin Self-Aligned SiC Nanowire Arrays. *Nanomaterials*. 8, 906–906 (2018).

<sup>40</sup> M. G. Wood, L. Chen, J. R. Burr, R. M. Reano, Optimization of electron beam patterned hydrogen silsesquioxane mask edge roughness for low-loss silicon waveguides. *Journal of Nanophotonics*. 8, 083098–083098 (2014).

<sup>41</sup> K. Groot-Berning, T. Kornher, G. Jacob, F. Stopp, S. T. Dawkins, R. Kolesov, Jörg Wrachtrup, K. Singer, F. Schmidt-Kaler, Deterministic Single-Ion Implantation of Rare-Earth Ions for Nanometer-Resolution Color-Center Generation. *Physical Review Letters*. 123 (2019), doi:<https://doi.org/10.1103/physrevlett.123.106802>.

<sup>42</sup> J. Lee, V. Leong, D. Kalashnikov, J. Dai, A. Gandhi, L. A. Krivitsky, Integrated single photon emitters. *AVS Quantum Science*. 2, 031701 (2020).

<sup>43</sup> I. Aharonovich, D. Englund, M. Toth, Solid-state single-photon emitters. *Nature Photonics*. 10, 631–641 (2016).

<sup>44</sup> “Amplitude Modulation Application note: AM input,” (available at <https://purephotonics.com/wp-content/uploads/Application-note-AM-input.pdf>).

<sup>45</sup> A. M. Dibos, M. T. Solomon, S. E. Sullivan, M. K. Singh, K. E. Sautter, C. P. Horn, G. D. Grant, Y. Lin, J. Wen, F. Joseph Heremans, S. Guha, D. D. Awschalom, Purcell Enhancement of Erbium Ions in TiO<sub>2</sub> on Silicon Nanocavities. *Nano Letters*. 22, 6530–6536 (2022).

<sup>46</sup> A. Kaloyerous, S. Dutta, S. Gallis, Engineering and polarization properties of erbium-implanted lithium niobate films for integrated quantum applications. *APL Materials*. 12 (2024), doi:<https://doi.org/10.1063/5.0220106>.

<sup>47</sup> S. Gallis, M. Huang, A. E. Kaloyerous, Efficient energy transfer from silicon oxycarbide matrix to Er ions via indirect excitation mechanisms. *Applied Physics Letters*. 90 (2007), doi:<https://doi.org/10.1063/1.2730583>.

<sup>48</sup> S. Gallis, V. Nikas, H. Suhag, M. Huang, A. E. Kaloyerous, White light emission from amorphous silicon oxycarbide (a-SiCxOy) thin films: Role of composition and postdeposition annealing. *Applied Physics Letters*. 97 (2010), doi:<https://doi.org/10.1063/1.3482938>.

<sup>49</sup> B. Ford, N. Tabassum, V. Nikas, S. Gallis, Strong Photoluminescence Enhancement of Silicon Oxycarbide through Defect Engineering. *Materials*. 10, 446 (2017).

---

<sup>50</sup> S. Gallis, V. Nikas, A. E. Kaloyerous, Silicon Oxycarbide Thin films and Nanostructures: Synthesis, Properties and Applications. Modern Technologies for Creating the Thin-film Systems and Coatings (2017), doi:<https://doi.org/10.5772/66992>.

<sup>51</sup> X. Fu, S. Fu, Q. Lu, J. Zhang, P. Wan, J. Liu, Y. Zhang, C.-H. Chen, W. Li, H. Wang, Q. Mei, Excitation energy mediated cross-relaxation for tunable upconversion luminescence from a single lanthanide ion. *Nature Communications*. 13 (2022), doi:<https://doi.org/10.1038/s41467-022-32498-4>.

<sup>52</sup> C. Zhu, M. Marczak, L. Feld, S. C. Boehme, C. Bernasconi, A. Moskalenko, I. Cherniukh, D. Dirin, M. I. Bodnarchuk, M. V. Kovalenko, G. Rainò, Room-Temperature, Highly Pure Single-Photon Sources from All-Inorganic Lead Halide Perovskite Quantum Dots. *Nano Letters*. 22, 3751–3760 (2022).

<sup>53</sup> W. Akhtar, T. Sekiguchi, T. Itahashi, V. Filidou, J. J. L. Morton, L. Vlasenko, K. M. Itoh, Rabi oscillation and electron-spin-echo envelope modulation of the photoexcited triplet spin system in silicon. *Physical Review B*. 86 (2012), doi:<https://doi.org/10.1103/physrevb.86.115206>.

[54] J.-F. Wang, F.-F. Yan, Q. Li, Z.-H. Liu, H. Liu, G.-P. Guo, L.-P. Guo, X. Zhou, J.-M. Cui, J. Wang, Z.-Q. Zhou, X.-Y. Xu, J.-S. Xu, C.-F. Li, G.-C. Guo, Coherent Control of Nitrogen-Vacancy Center Spins in Silicon Carbide at Room Temperature. *Physical Review Letters*. 124 (2020), doi:<https://doi.org/10.1103/physrevlett.124.223601>.

[55] G. Wolfowicz, C. P. Anderson, Berk Diler, O. G. Poluektov, F. Joseph Heremans, D. D. Awschalom, Vanadium spin qubits as telecom quantum emitters in silicon carbide. *Science advances*. 6 (2020), doi:<https://doi.org/10.1126/sciadv.aaz1192>.

[56] D. J. Christle, P. V. Klimov, Charles, Krisztián Szász, Viktor Ivády, Valdas Jokubavicius, J. U. Hassan, Mikael Syväjärvi, W. F. Koehl, Takeshi Ohshima, N. T. Son, E. Janzén, Á. Gali, D. D. Awschalom, Isolated Spin Qubits in SiC with a High-Fidelity Infrared Spin-to-Photon Interface. *Physical Review X*. 7 (2017), doi:<https://doi.org/10.1103/physrevx.7.021046>.

[57] Y. Zhou, Z. Wang, A. Rasmita, S. Kim, A. Berhane, Z. Bodrog, G. Adamo, A. Gali, I. Aharonovich, W. Gao, Room temperature solid-state quantum emitters in the telecom range. *Science Advances*. 4 (2018), doi:<https://doi.org/10.1126/sciadv.aar3580>.

[58] W. Redjem, A. Durand, T. Herzog, A. Benali, S. Pezzagna, J. Meijer, A. Yu. Kuznetsov, H. S. Nguyen, S. Cueff, J.-M. Gérard, I. Robert-Philip, B. Gil, D. Caliste, P. Pochet, M. Abbarchi, V. Jacques, A. Dréau, G. Cassabois, Single artificial atoms in silicon emitting at telecom wavelengths. *Nature electronics*. 3, 738–743 (2020).

[59] Y. Baron, A. Durand, P. Udvarhelyi, T. Herzog, M. Khouri, S. Pezzagna, J. Meijer, I. Robert-Philip, M. Abbarchi, J.-M. Hartmann, V. Mazzocchi, J.-M. Gérard, A. Gali, V. Jacques, G. Cassabois, A. Dréau, Detection of Single W-Centers in Silicon. *ACS Photonics*. 9, 2337–2345 (2022).

[60] A. Durand, Y. Baron, W. Redjem, T. Herzog, A. Benali, S. Pezzagna, J. Meijer, A. Yu Kuznetsov, J.-M. Gérard, I. Robert-Philip, M. Abbarchi, V. Jacques, G. Cassabois, A. Dréau, Broad Diversity of Near-Infrared Single-

---

Photon Emitters in Silicon. Physical Review Letters. 126 (2021), doi:<https://doi.org/10.1103/physrevlett.126.083602>.

[61] J.-S. Chen, K. J. Trerayapiwat, L. Sun, M. D. Krzyaniak, M. R. Wasielewski, T. Rajh, S. Sharifzadeh, X. Ma, Long-lived electronic spin qubits in single-walled carbon nanotubes. *Nature Communications*. 14 (2023), doi:<https://doi.org/10.1038/s41467-023-36031-z>.

[62] M. Hollenbach, N. Klingner, N. S. Jagtap, L. Bischoff, C. Fowley, Ulrich Kentsch, Gregor Hlawacek, A. Erbe, N. V. Abrosimov, M. Helm, Yonder Berencén, G. V. Astakhov, Wafer-scale nanofabrication of telecom single-photon emitters in silicon. *Nature Communications*. 13 (2022), doi:<https://doi.org/10.1038/s41467-022-35051-5>.

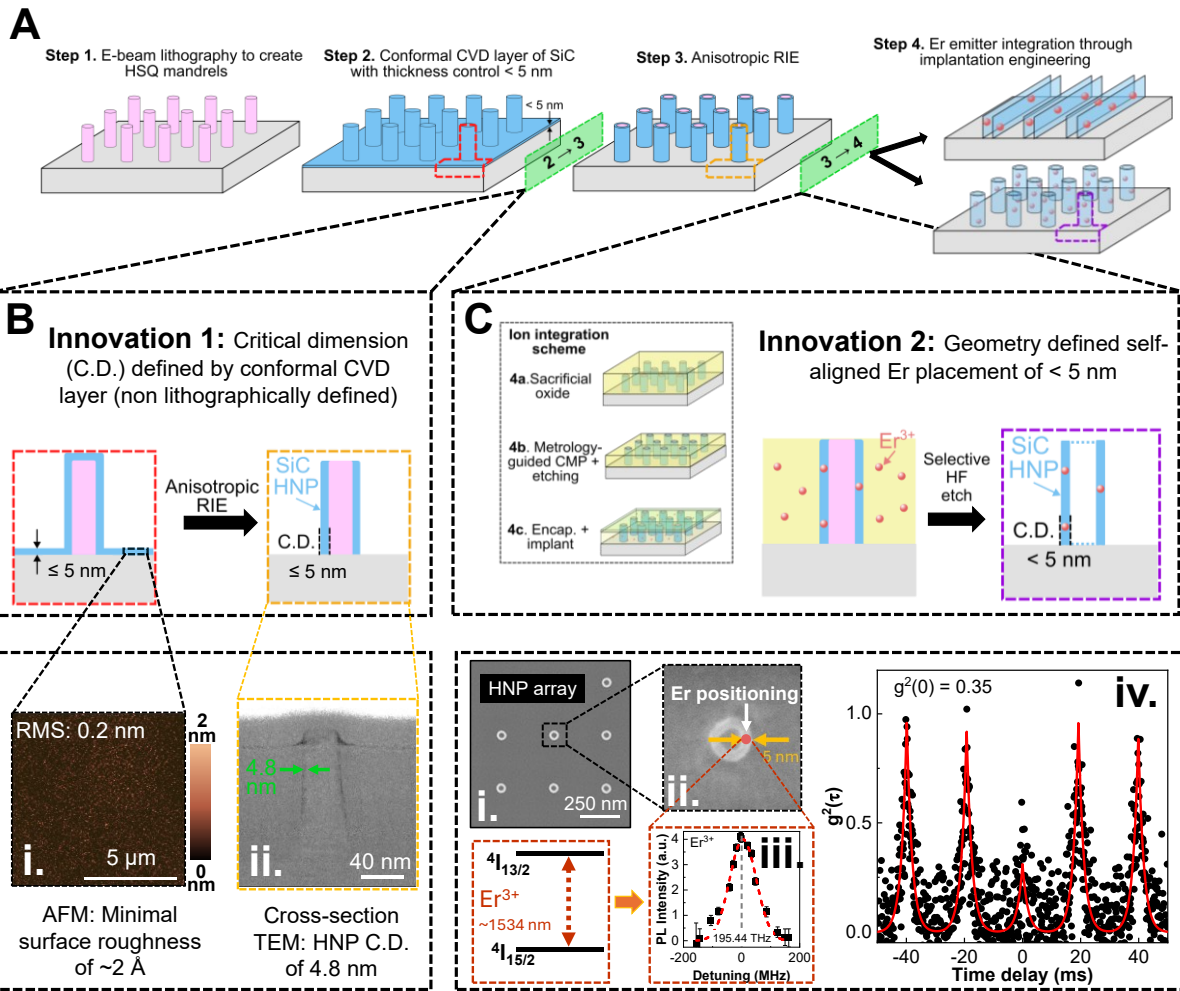


**Figure 1: Key-enabling nanofabrication for deterministic integration of single-Er-ions in SiC hollow nanopillar (HNP) arrays. (A)** Nanofabrication sequence and innovations for Er in engineered SiC (doped with oxygen) nanostructures, including HNP and NW arrays. **(B)** *Innovation 1:* Highly conformal SiC CVD enables C.D. control below lithographic resolution limits ( $\leq 5$  nm), defined by SiC layer thickness rather than lithography. **i.** AFM image of SiC films showing RMS roughness of  $\sim 2$  Å. **ii.** Cross sectional TEM of an HNP with a C.D. (sidewall) of  $\sim 4.8$  nm. **(C)** *Innovation 2:* Geometry-driven self-aligned ion placement, where the nanostructure sidewall serves as an implantation aperture, confining ions with  $< 5$  nm accuracy. **i.** Top-down SEM image of a representative  $3 \times 4$  HNP array. and **ii.** a single HNP highlighting Er confinement within the  $\sim 5$  nm sidewall. **iii.** Room-temperature PLE spectrum of a single- $\text{Er}^{3+}$  in a  $3 \times 4$  HNP array exhibiting the distinct telecom C-band optical  $Z_1 - Y_1$  transition  $\sim 195.44$  THz ( $\sim 1533.9$  nm) with a linewidth of  $\sim 67$  MHz, limited by the tunable laser. **iv.** Corresponding  $g^2$  correlation measurement showing a  $g^2(0) = 0.35$ , confirming isolation of a spatially resolved single  $\text{Er}^{3+}$  ion.

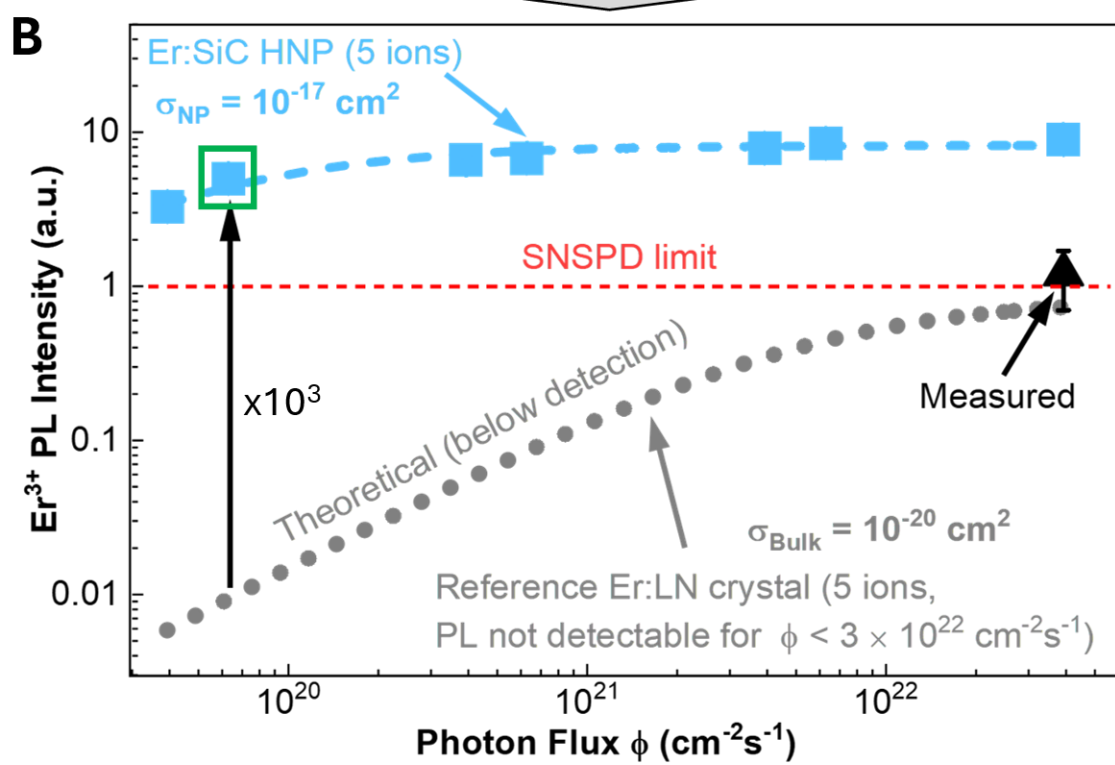
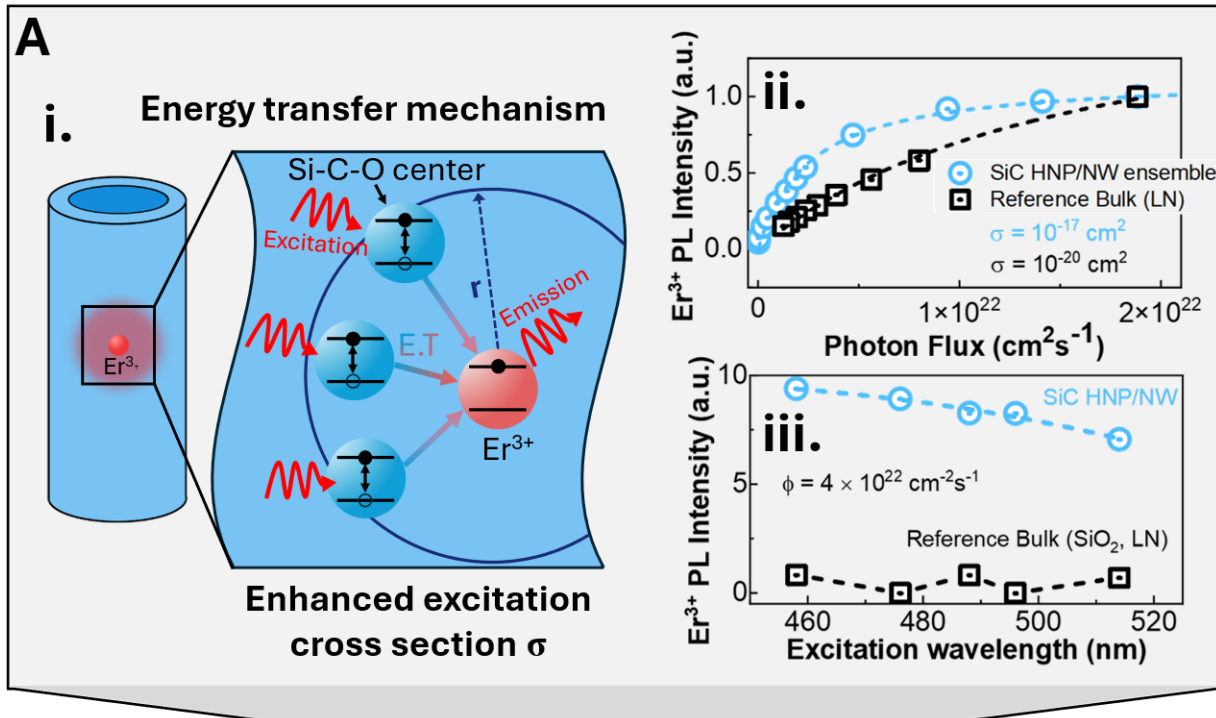


**Figure 2: Enhanced excitation cross-section,  $\sigma$ , for  $\text{Er}^{3+}$  in SiC HNP arrays enabling room-temperature single- $\text{Er}^{3+}$ -ion detection.** **(A)** **i.** Schematic illustrating the matrix-assisted energy excitation in Er:SiC nanostructures. Efficient energy transfer is enabled by Si-C-O centers in SiC via energy states that overlap with the  $\text{Er}^{3+}$  excited-state manifold. **ii.** Telecom-PDPL studies and fits demonstrate that ensemble  $\text{Er}^{3+}$  in the SiC HNP/NW has  $\sigma \approx 2 \times 10^{-17} \text{ cm}^2$ , which is 2-3 orders higher than typical values in bulk rare-earth hosts; for example, as seen in the Er-implanted LN thin films (reference). **iii.** Broadband excitation behavior of ensemble  $\text{Er}^{3+}$  in SiC HNP/NW compared to ensemble bulk reference (Er:LN and Er:SiO<sub>2</sub>), as demonstrated by PLE at non-resonant (476 nm and 496 nm) excitations while monitoring the telecom emission. **(B)** Representative  $\text{Er}^{3+}$ -PL from Er:SiC HNP array, containing  $\sim 5 \text{ Er}^{3+}$ , exhibits an intensity  $\sim 3$  orders of magnitude higher than the calculated intensity from the reference at the primary photon-flux ( $\phi \sim 5 \times 10^{19} \text{ cm}^{-2} \cdot \text{s}^{-1}$ ) used in the experiments (telecom-resonant excitation  $\sim 1533.9 \text{ nm}$ ). In contrast, the PL in the reference, with an equivalent number of Er ions, remains essentially undetectable even at the highest excitation photon flux used,  $\phi > 4 \times 10^{22} \text{ cm}^{-2} \cdot \text{s}^{-1}$ , a three-order higher value than the primary flux.

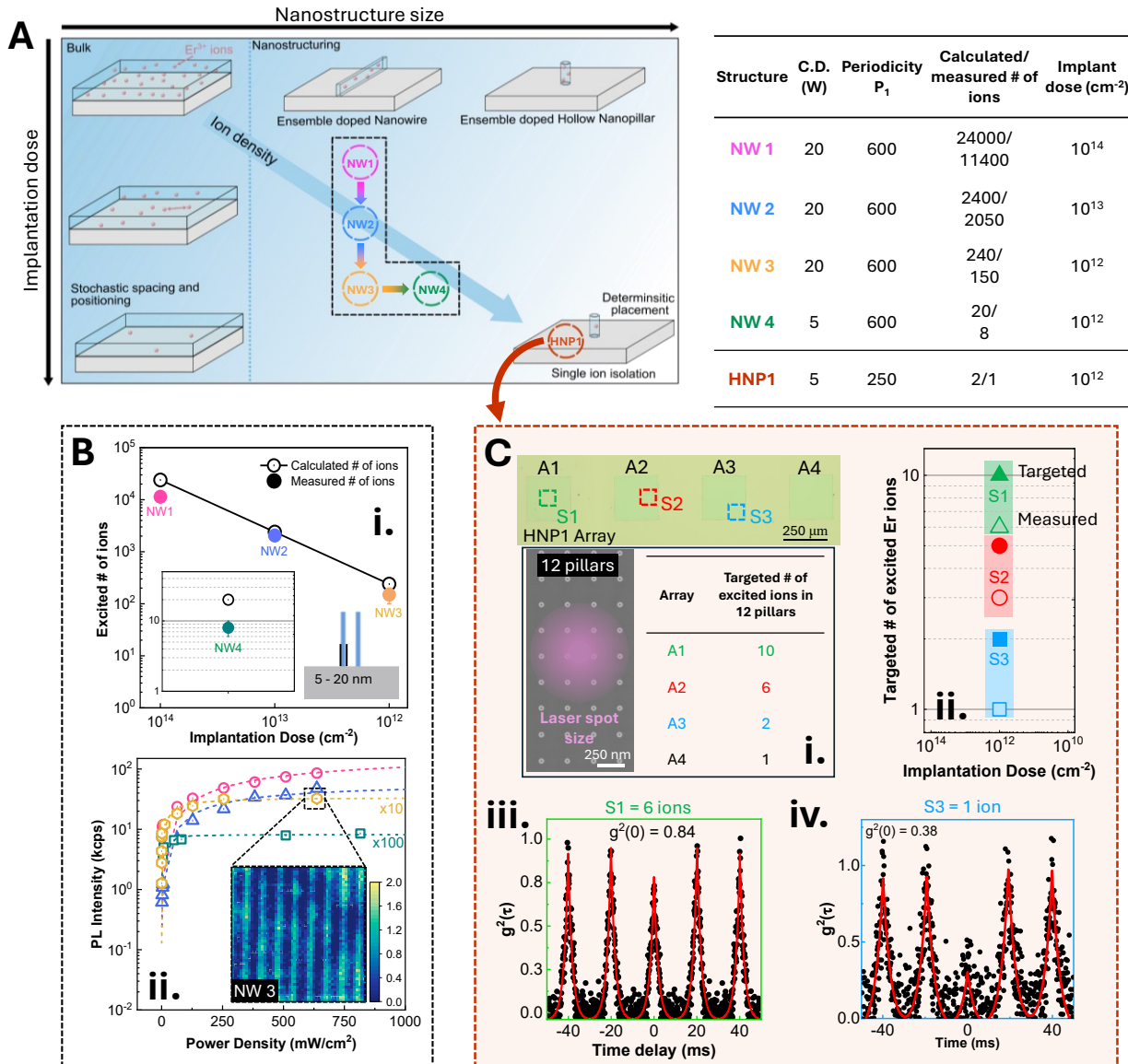


**Figure 3: Blueprint for spatially-resolved single-ion isolation in SiC HNP arrays.** **A.** A combined nanostructuring and implantation strategy enables deterministic isolation of single  $\text{Er}^{3+}$ . Starting from a bulk/thin-film SiC host with randomly distributed Er ions, SiC HNP geometries confine ions laterally and reduce the effective ion density within the optical excitation volume. By tuning implantation dose (y-axis) and C.D. or number of nanostructures (x-axis), the system transitions from ensemble excitation to single-ion isolation. Fabricated NW calibration structures NW1-NW4 and HNP1 serve as experimental testbeds, with calculated and validated ion counts summarized in the accompanying Table. **B. i.** Quantitative validation in NW arrays shows strong agreement between predicted and experimentally extracted number of ions. **ii.** PL saturation confirms emitter density reduction: arrays implanted at  $10^{14} \text{ cm}^{-2}$  yield  $\sim 180$  kcps, while  $10^{12} \text{ cm}^{-2}$  arrays exhibit  $\sim 0.08$  kcps, consistent with excitation of only a few ions. Confocal telecom PL maps illustrate the shift from bright ensemble emission to isolated sites. **C. i.** For HNP arrays, four designs (A1–A4) target 10, 6, 2, and 1 optically-active  $\text{Er}^{3+}$ -ions within a  $4 \times 3$  array. **ii.** Representative  $g^2(\tau)$  measurements, with  $g^2(0)$  values ranging from 0.84 (multi-ion, S1) to 0.38 (S3), demonstrating successful isolation of a spatially-resolved single  $\text{Er}^{3+}$ .

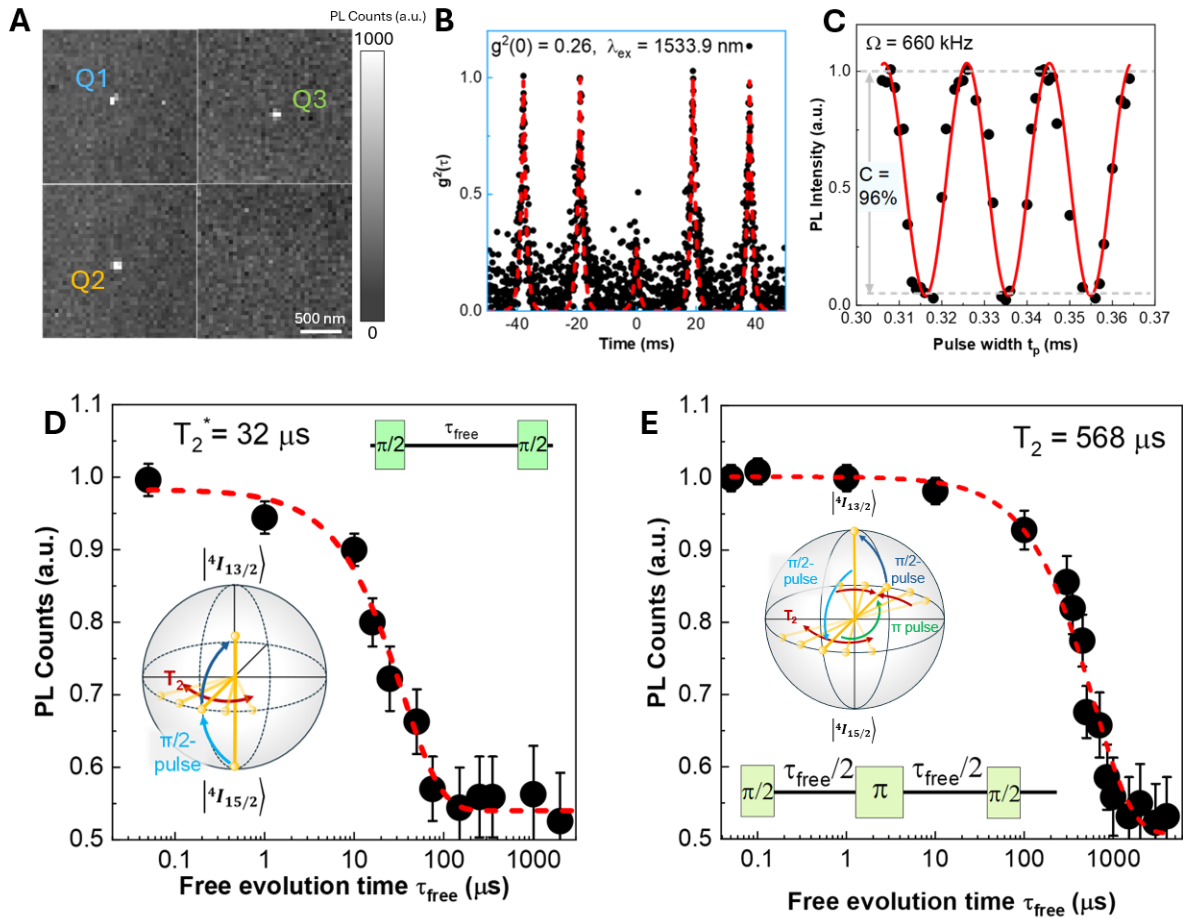


**Figure 4: Room temperature properties of single-Er SiC HNP devices in the telecom-C band.** **A.** Upconversion-enabled PL camera images demonstrating spatial-isolation of single-Er<sup>3+</sup>-qudits Q1, Q2, Q3, and background counts on the HNP1 (A4). **B.**  $g^2(\tau)$  measurements for Q1 show pronounced antibunching under  $\sim$ 1534 nm excitation with  $g^2(0) = 0.26$ , demonstrating telecom C-band single-photon emission. **C.** Rabi measurements on Q1 demonstrate coherent Rabi oscillations of the optical transition ( $\Omega_{Rabi} = 660$  kHz with contrast  $>96\%$ ). **D.** Ramsey spectroscopy on Q1 of the telecom Er transition: Integrated intensity decay of the Er<sup>3+</sup> emission after the Ramsey sequences. The inset schematically shows the decoherence process of the single-Er<sup>3+</sup> ion excited by a  $\pi/2$  pulse; the dark-blue arrow indicates the second  $\pi/2$  pulse of the Ramsey pair, which projects the single-Er<sup>3+</sup> state onto the excited state. The extracted decay time  $T_2^*$  from a single-exponential fit is 32  $\mu$ s. **E.** Corresponding standard photon-echo measurements varying the inter-pulse free-evolution time ( $\tau_{\text{free}}/2$ ) with the pulse sequence used (inset). A final  $\pi/2$  pulse is applied to project the resulting refocused single-Er<sup>3+</sup> onto the excited- or coherent-superposition-state. The photon-echo fit reveals  $T_2 = \sim 568$   $\mu$ s.

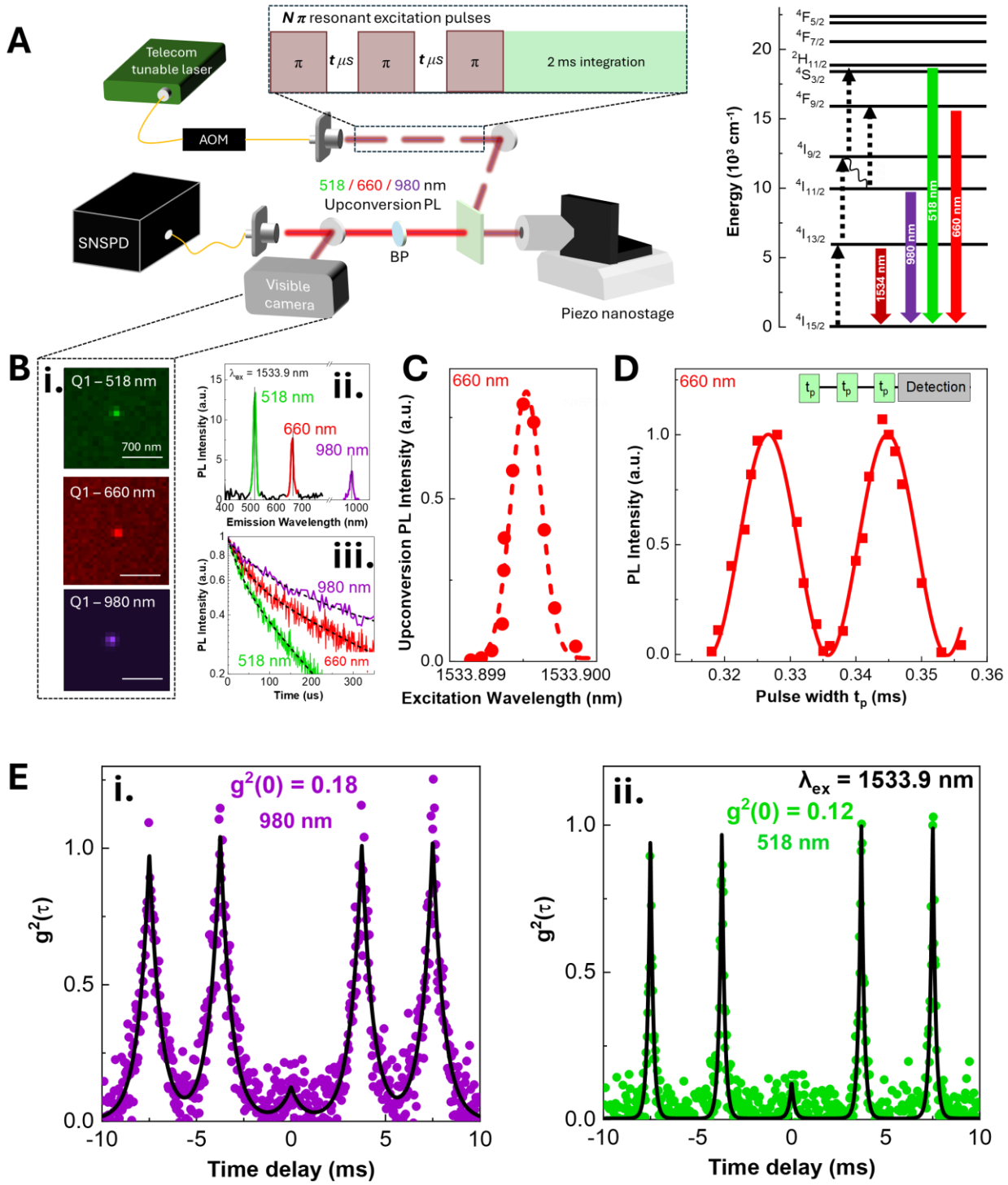


**Figure 5: Upconversion-mediated control of the visible and NIR states of single-Er<sup>3+</sup> qudits (5-level system).** **A.** Schematic of the measurement setup for upconversion-mediated PL and microscopy from single-Er<sup>3+</sup> qudits. Energy-level diagram for trivalent Er<sup>3+</sup> showing the telecom ( $\sim 1534$  nm) as well as its distinct visible ( $\sim 518$ ,  ${}^4I_{15/2} \leftrightarrow {}^2H_{11/2}$ , and  $\sim 660$  nm,  ${}^4I_{15/2} \leftrightarrow {}^4F_{9/2}$ ) and NIR ( $\sim 980$  nm,  ${}^4I_{15/2} \leftrightarrow {}^4I_{11/2}$ ) optical transitions, involved in Er<sup>3+</sup> luminescence. **(B)** Upconversion PL characterization of a single-Er<sup>3+</sup> qudit (Q1). **i.** Upconversion-mediated optical microscopy showing a sub-diffraction background-free bright spot corresponding to an individually-addressable Er<sup>3+</sup>-ion at three different wavelengths (518 nm, 660 nm, 980 nm). **ii.** Upconversion PL spectra showing emission at 518 nm, 660 nm, and 980 nm, with **iii.** lifetimes of 164  $\mu$ s, 380  $\mu$ s, and 712  $\mu$ s, respectively. **C.** Representative PLE with extracted optical linewidth of Q1 obtained via upconversion detection at 660 nm exhibits an optical linewidth of  $\sim 37$  MHz at room temperature (laser-broadening limited). **D.** Upconversion PL at 660 nm demonstrating Rabi oscillations under resonant excitation. **E.** Multiwavelength, background-free and enhanced single-photon emission demonstrated for the single-Er<sup>3+</sup> qudit at **i.** 980 nm with  $g^2(0) = 0.18$ , and **ii.** 518 nm with  $g^2(0) = 0.12$ .